View metadata, citation and similar papers at core.ac.uk

brought to you by CORE

provided by NASA Technical Reports Server

NASA-CR-203119

Radio Science, Volume 30, Number 4, Pages 835–852, July–August 1995

Polarimetric scattering from layered media with multiple species of scatterers

S. V. Nghiem, R. Kwok, and S. H. Yueh

Jet Propulsion Laboratory, California Institute of Technology, Pasadena

J. A. Kong, C. C. Hsu, M. A. Tassoudji, and R. T. Shin

Department of Electrical Engineering and Computer Science and Research Laboratory of Electronics
Massachusetts Institute of Technology, Cambridge

Abstract. Geophysical media are usually heterogeneous and contain multiple species of scatterers. In this paper a model is presented to calculate effective permittivities and polarimetric backscattering coefficients of multispecies-layered media. The same physical description is consistently used in the derivation of both permittivities and scattering coefficients. The strong permittivity fluctuation theory is extended to account for the multiple species of scatterers with a general ellipsoidal shape whose orientations are randomly distributed. Under the distorted Born approximation, polarimetric scattering coefficients are obtained. These calculations are applicable to the special cases of spheroidal and spherical scatterers. The model is used to study effects of scatterer shapes and multispecies mixtures on polarimetric signatures of heterogeneous media. The multispecies model accounts for moisture content in scattering media such as snowpack in an ice sheet. The results indicate a high sensitivity of backscatter to moisture with a stronger dependence for drier snow and ice grain size is important to the backscatter. For frost-covered saline ice, model results for bare ice are compared with measured data at C band and then the frost flower formation is simulated with a layer of fanlike ice crystals including brine infiltration over a rough interface. The results with the frost cover suggest a significant increase in scattering coefficients and a polarimetric signature closer to isotropic characteristics compared to the thin saline ice case.

1. Introduction

Natural geophysical media are usually inhomogeneous and contain various species of scatterers with different sizes, shapes, and permittivities. Much of the early work on multispecies media focused on calculations of effective permittivities. A multiphase dielectric mixture theory was presented by *Tinga et al.* [1973] with a summary of most important mixture relations derived by many authors. In a study of heterogeneous earth media such as brine-saturated rocks, it was found that the particle shape plays a major role in the effective electrical properties characterized by mixing formulas [*Wait*, 1983]. Expressions for effective permittivities of media with multiphase ellipsoids have been derived by *Sihvola and Kong* [1988], whose results lead to generalized Lorentz-Lorenz, Polder–van Santen, and coherent potential quasi-crystalline approximation formulas with applications to snow and sea ice.

The above formulations account for absorption loss in the inhomogeneous media. To include scattering effects, the strong permittivity fluctuation theory is used to calculate effective permittivities of multispecies media such as dry and wet snow and vegetation [*Tsang and Kong*, 1981a, b; *Tsang et al.*, 1982]. For sea ice containing brine and air inclusions, effective permittivities are computed with the strong fluctuation theory at microwave frequencies [*Stogryn*, 1987]. For multispecies media with densely distributed particles, effective propagation constants are obtained for spherical scatterers under quasi-crystalline and quasi-crystalline with coherent potential approximations [*Ding and Tsang*, 1989].

Effective permittivities describe wave propagation and attenuation in inhomogeneous media. However, to interpret physical characteristics of

Copyright 1995 by the American Geophysical Union.

Paper number 95RS01247.
0048-6604/95/95RS-01247$08.00

the media from remote sensing radar data, electromagnetic scattering from multiple species of scatterers needs to be derived. Conventional backscattering coefficients are calculated with a model of sea ice containing spherical scatterers in isotropic media with rough surfaces [*Tjuatja et al.*, 1992]. Polarimetric signatures of sea ice are derived with a model for ellipsoidal inclusions embedded in anisotropic layered media with rough interfaces [*Nghiem et al.*, 1993b]. These models consider a single species of scatterers (two-phase mixture) and are applicable when the inhomogeneities are dominantly consisted of scatterers of the same types. It is shown with a theoretical model of forest backscatter [*Lang et al.*, 1993] that different species with different permittivities and structures can cause large variations in backscattering coefficients of pine trees for vertical polarization at C band. Polarimetric signatures of a layer of multispecies spheroidal scatterers are also studied based on vector radiative transfer theory [*Tsang et al.*, 1990].

In this paper, both effective permittivities and polarimetric signatures are derived from the same physical description of inhomogeneous layered media. The difference with the above-referenced papers is that this present work presents a consistent model for wave propagation, attenuation, and polarimetric scattering under the framework of the analytic wave theory, which simultaneously considers multiple species, ellipsoidal shape, large permittivity differences, absorption and scattering losses, preservation of phase information, multiple interactions with layer boundaries, and polarimetric signatures of the heterogeneous media. Effective permittivities are derived with random orientations of the multispecies nonspherical scatterers. The distorted Born approximation is applied to calculate polarimetric scattering coefficients in the covariance matrix [*Nghiem et al.*, 1990]. These calculations involve numerical integrations over Eulerian angles; however, analytical expressions are also obtained under the low-frequency approximation. Polarimetric signatures of media with multispecies mixing and various scatterer shapes are presented in examples for vegetation, snow, ice sheet, and sea ice.

2. Effective Permittivity

The effective permittivity of a heterogeneous medium is composed of a quasi-static part and a scattering effect part corresponding to the first and second terms, respectively, in the following expression [*Tsang and Kong*, 1981a]

$$\bar{\bar{\varepsilon}}_{\text{eff}} = \bar{\bar{\varepsilon}}_g + \varepsilon_0[\bar{\bar{I}} - \bar{\bar{\xi}}_{\text{eff}} \cdot \langle \bar{\bar{S}} \rangle]^{-1} \cdot \bar{\bar{\xi}}_{\text{eff}} \tag{1}$$

where $\bar{\bar{I}}$ is the unit dyad, ε_0 is the permittivity of free space, $\bar{\bar{\varepsilon}}_g$ is an auxiliary permittivity, and $\bar{\bar{S}}$ is a dyadic coefficient. For a medium containing N species, effective dyadic scatterer $\bar{\bar{\xi}}_{\text{eff}}$ is given by

$$[\bar{\bar{\xi}}_{\text{eff}}]_{jm} = \sum_{i=1}^{N} \int_0^{2\pi} d\gamma \int_0^{\pi} d\beta \int_0^{2\pi} d\alpha \, p(\alpha, \beta, \gamma) \sum_{k,l}^{x,y,z} \Gamma^{(0)}_{i\xi jklm} \cdot \left\{ k_0^2 \int_{-\infty}^{\infty} d\bar{k}' \, [\bar{\bar{G}}_g(\bar{k}')]_{kl} \Phi_{i\xi}(\bar{k}') + [\bar{\bar{S}}_i]_{kl} \right\} \Big|_{\alpha,\beta,\gamma} \tag{2}$$

under the condition $|[\bar{\bar{\xi}}_{\text{eff}}]|_{jm} \ll 1$. In (2), subscript i stands for species i, k_0 is the wave number in free space, $\Gamma^{(0)}_{i\xi jklm}$ is the variance of the scattering fluctuations (determined by (6) below), and $p(\alpha, \beta, \gamma)$ is the probability density function of orientations given by Eulerian angles α, β, and γ. In this paper the random orientation distribution of the multispecies scatterers is considered. This requires the isotropic form of the Green's function $\bar{\bar{G}}_g$ [*Nghiem et al.*, 1990], and the auxiliary permittivity tensor becomes $\bar{\bar{\varepsilon}}_g = \varepsilon_g \bar{\bar{I}}$.

The size and shape of scatterer species i are described with the Fourier transform $\Phi_{i\xi}(\bar{k}')$ of the normalized local correlation function. For ellipsoids, $\Phi_{i\xi}(\bar{k}')$ takes on the form

$$\Phi_{i\xi}(\bar{k}') = \frac{\ell_{ix'} \ell_{iy'} \ell_{iz'}}{\pi^2 (1 + k_x'^2 \ell_{ix'}^2 + k_y'^2 \ell_{iy'}^2 + k_z'^2 \ell_{iz'}^2)^2} \tag{3}$$

in which $\ell_{ix'}$, $\ell_{iy'}$, and $\ell_{iz'}$ are three different correlation lengths in the local coordinates corresponding to the minor, the meridian, and the major axes of an ellipsoidal scatterer of species i. The local principal coordinate system (x', y', z') of an ellipsoid is related to the global coordinate system (x, y, z) by Eulerian angles α, β, and γ as shown in Appendix A.

To facilitate the derivation, the following principal variances are defined in the local coordinates as

$$\delta_{i\xi j'k'} = \delta_{i\xi k'j'} = f_{si} f_b (\xi_{ij'} - \xi_{bj'})(\xi_{ik'} - \xi_{bk'}) \tag{4}$$

where $j', k' = x', y', z'$, subscript si denotes scatterer (indicated by s) species i, subscript b is for

the background medium, and the following definitions have been used

$$\xi_{ix'} = \frac{\varepsilon_{si} - \varepsilon_g}{\varepsilon_0 + S_{ix'}(\varepsilon_{si} - \varepsilon_g)} \tag{5a}$$

$$\xi_{iy'} = \frac{\varepsilon_{si} - \varepsilon_g}{\varepsilon_0 + S_{iy'}(\varepsilon_{si} - \varepsilon_g)} \tag{5b}$$

$$\xi_{iz'} = \frac{\varepsilon_{si} - \varepsilon_g}{\varepsilon_0 + S_{iz'}(\varepsilon_{si} - \varepsilon_g)} \tag{5c}$$

For the background, (5) is used with subscript i replaced by b and species permittivity ε_{si} by background permittivity ε_b. In the global coordinates the Eulerian transformation rotates the principal variances $\delta_{i\xi j'k'}$ to

$$\begin{aligned}\Gamma^{(0)}_{i\xi jklm} &= \delta_{i\xi x'x'}a_{xjk}a_{xlm} + \delta_{i\xi x'y'}a_{xjk}a_{ylm} + \delta_{i\xi x'z'}a_{xjk}a_{zlm} \\ &+ \delta_{i\xi y'x'}a_{yjk}a_{xlm} + \delta_{i\xi y'y'}a_{yjk}a_{ylm} + \delta_{i\xi y'z'}a_{yjk}a_{zlm} \\ &+ \delta_{i\xi z'x'}a_{zjk}a_{xlm} + \delta_{i\xi z'y'}a_{zjk}a_{ylm} + \delta_{i\xi z'z'}a_{zjk}a_{zlm}\end{aligned} \tag{6}$$

where a_{jkl}'s have been defined in Appendix B.

The condition of secular elimination is used to derive ε_g and $\bar{\bar{S}}$ [*Tsang et al.*, 1981a; *Yueh et al.*, 1990; *Nghiem et al.*, 1993a, b]. This condition imposes $\bar{\bar{\xi}}(\bar{r})\rangle = 0$ where the ensemble average is obtained by

$$\langle\bar{\bar{\xi}}(\bar{r})\rangle = \int_0^{2\pi} d\gamma \int_0^{\pi} d\beta \int_0^{2\pi} d\alpha\, p(\alpha, \beta, \gamma)\bar{\bar{T}}^{-1} \cdot \left[f_b\bar{\bar{\xi}}_b + \sum_{i=1}^{N} f_{si}\bar{\bar{\xi}}_i \right] \cdot \bar{\bar{T}} \tag{7}$$

In (7) the probability density function of orientations for randomly oriented scatterers is

$$p(\alpha, \beta, \gamma) = \sin\beta/(8\pi^2) \tag{8}$$

which renders $\bar{\bar{\varepsilon}}_g$ isotropic. As shown in Appendix B, this orientation distribution together with the secular elimination condition cast (7) into

$$f_b(\xi_{bx'} + \xi_{by'} + \xi_{bz'}) + \sum_{i=1}^{N} f_{si}(\xi_{ix'} + \xi_{iy'} + \xi_{iz'}) = 0 \tag{9}$$

where ξ's have been defined by (5). Elements of $\bar{\bar{S}}_i$ are calculated with the removal of the frequency independent parts in the effective scatterer terms as required by the secular elimination condition. Applying the symmetry of the ellipsoidal function leads to the following results

$$S_{iz'}(\ell_{ix'}, \ell_{iy'}, \ell_{iz'}) = \int_0^{2\pi} d\phi \frac{\varepsilon_0(1 + a_i)}{2\pi\varepsilon_g a_i\sqrt{a_i}}[\sqrt{a_i} - \tan^{-1}\sqrt{a_i}] \tag{10a}$$

$$S_{iy'}(\ell_{ix'}, \ell_{iy'}, \ell_{iz'}) = S_{iz'}(\ell_{ix'}, \ell_{iz'}, \ell_{iy'}) \tag{10b}$$

$$S_{ix'}(\ell_{ix'}, \ell_{iy'}, \ell_{iz'}) = S_{iz'}(\ell_{iz'}, \ell_{iy'}, \ell_{ix'}) \tag{10c}$$

where principal branch cuts and principal Riemann sheets have been chosen for the square root and the inverse tangent functions. In (10) the integrations over ϕ can be carried out numerically and a_i and γ_i are defined as

$$a_i = \gamma_i^2 - 1 \tag{11a}$$

$$\gamma_i = \left(\frac{\cos^2\phi}{\gamma_{ix'}^2} + \frac{\sin^2\phi}{\gamma_{iy'}^2}\right)^{-1/2} \tag{11b}$$

$$\gamma_{ix'} = \frac{\ell_{ix'}}{\ell_{iz'}} \qquad \gamma_{iy'} = \frac{\ell_{iy'}}{\ell_{iz'}} \tag{11c}$$

Then, the average dyadic coefficient $\langle\bar{\bar{S}}\rangle$ in (1) is determined by

$$\begin{aligned}\langle\bar{\bar{S}}\rangle &= \sum_{i=1}^{N,b} f_{si} \int_0^{2\pi} d\gamma \int_0^{\pi} d\beta \int_0^{2\pi} d\alpha\, p(\alpha, \beta, \gamma)\bar{\bar{T}}^{-1} \\ &\cdot \begin{bmatrix} S_{ix'} & 0 & 0 \\ 0 & S_{iy'} & 0 \\ 0 & 0 & S_{iz'} \end{bmatrix} \cdot \bar{\bar{T}} = \frac{f_b}{3}(S_{bx'} + S_{bz'} + S_{bz'})\bar{\bar{I}} \\ &+ \sum_{i=1}^{N} \frac{f_{si}}{3}(S_{ix'} + S_{iz'} + S_{iz'})\bar{\bar{I}} = S\bar{\bar{I}}\end{aligned} \tag{12}$$

where $\bar{\bar{S}}_b = \sum f_{si}\bar{\bar{S}}_i/\sum f_{si}$. Equations (9) and (12) are used to solve for ε_g and S's with an iteration method.

To complete the calculation of the effective permittivity, let the quantity in the brackets in (2) be

$$\eta_{ijm}(\bar{r}') = k_0^2 \int_{-\infty}^{\infty} d\bar{k}'\, [\bar{\bar{G}}_g(\bar{k}')]_{kl}\Phi_{i\xi}(\bar{k}') + [\bar{\bar{S}}_i]_{kl} \tag{13}$$

In the local coordinates, $\bar{\bar{\eta}}_i(\hat{r}')$ is a diagonal tensor whose elements are

$$\eta_{ij'j'} = \eta_{ij'} = I_{ij'} + S_{ij'}, \qquad j' = x', y', z' \tag{14}$$

where $I_{ij'}$ involves the integration of dyadic Green's function and correlation function. The result for $I_{iz'}$ is

$$I_{iz'} = \int_0^{2\pi} d\phi \, \frac{-\varepsilon_0}{\pi \varepsilon_g} (\mathcal{I}_{i\phi}^s + \mathcal{I}_{i\phi}^d) \tag{15a}$$

$$\mathcal{I}_{i\phi}^s = -\frac{\gamma_i^3}{2a_i^2}\left[\frac{\sqrt{-\zeta}}{\vartheta_e} + \frac{\vartheta_e + \zeta}{\vartheta_e\sqrt{\vartheta_e}}\left(\frac{\pi}{2} - \tan^{-1}\frac{\sqrt{-\zeta}}{\sqrt{\vartheta_e}}\right)\right] \tag{15b}$$

$$\mathcal{I}_{i\phi}^d = \frac{\gamma_i^2}{2a_i^2}\left[\frac{1 + a_i\nu_{gz'}^2}{\vartheta_o} + \frac{\vartheta_o(a_i + 2) - (b + a_i\nu_{gz'}^2)}{\vartheta_o\sqrt{\vartheta_o}} \cdot \left(\frac{\pi}{2} - \tan^{-1}\frac{1}{\sqrt{\vartheta_o}}\right)\right] \tag{15c}$$

$$\nu_{gz'}^2 = k_g^2\ell_{iz'}^2, \quad k_g^2 = \omega^2\mu_0\varepsilon_g, \quad \zeta = \gamma_i^2\nu_{gz'}^2 \tag{15d}$$

$$b = \frac{\gamma_i^2 + \zeta}{a_i}, \quad \vartheta_o = b - 1, \quad \vartheta_e = b + \zeta \tag{15e}$$

The symmetry of the ellipsoid is used again to find $I_{ix'}$ and $I_{iy'}$, which are simply

$$I_{ix'}(\ell_{ix'}, \ell_{iy'}, \ell_{iz'}) = I_{iz'}(\ell_{iz'}, \ell_{iy'}, \ell_{ix'}) \tag{16}$$

$$I_{iy'}(\ell_{ix'}, \ell_{iy'}, \ell_{iz'}) = I_{iz'}(\ell_{ix'}, \ell_{iz'}, \ell_{iy'}) \tag{17}$$

To rotate $\bar{\bar{\eta}}_i(\hat{r}')$ into the global coordinates, the Eulerian transformation is applied. Elements of $\bar{\bar{\eta}}_i(\hat{r})$ in the global coordinates are

$$\eta_{ikl} = \eta_{ix'}a_{xkl} + \eta_{iy'}a_{ykl} + \eta_{iz'}a_{zkl} = \eta_{ilk} \tag{18}$$

Variance Γ in (6) and quantity η in (18) are combined to define

$$\xi_{ijm}^{(0)} = \sum_{k,l}^{x,y,z} \Gamma_{i\xi jklm}^{(0)}\eta_{ikl} = \sum_{u,v,w}^{x,y,z} \delta_{i\xi u'v'}\eta_{iw'}(a_{uxj}a_{vxm}a_{wxx} + a_{uxj}a_{vym}a_{wxy} + a_{uxj}a_{vzm}a_{wxz} + a_{uyj}a_{vxm}a_{wyx} + a_{uyj}a_{vym}a_{wyy} + a_{uyj}a_{vzm}a_{wyz} + a_{uzj}a_{vxm}a_{wzx} + a_{uzj}a_{vym}a_{wzy} + a_{uzj}a_{vzm}a_{wzz}) \tag{19}$$

After the integration over the Eulerian angles for the terms in (19), the effective scatterer tensor for species i becomes

$$\bar{\bar{\xi}}_{i\text{eff}} = \int_0^{2\pi} d\gamma \int_0^{\pi} d\beta \int_0^{2\pi} d\alpha \; p(\alpha, \beta, \gamma)\bar{\bar{\xi}}_i^{(0)} = \tfrac{1}{3}(\delta_{i\xi x'x'}\eta_{ix'} + \delta_{i\xi y'y'}\eta_{iy'} + \delta_{i\xi z'z'}\eta_{iz'})\bar{\bar{I}} \tag{20}$$

Another method to find (20) is to carry out all tensor operations involving Γ's and η's in the local coordinates and then rotate the result into the global coordinates; Appendix B is readily applicable to arrive at (20). Substituting (20) in (2) and using the result in (1) yield the effective permittivity

$$\bar{\bar{\varepsilon}}_{\text{eff}} = \left[\varepsilon_g + \frac{\varepsilon_0}{3}\sum_{i=1}^{N}(\delta_{i\xi x'x'}\eta_{ix'} + \delta_{i\xi y'y'}\eta_{iy'} + \delta_{i\xi z'z'}\eta_{iz'})\right]\bar{\bar{I}} \tag{21}$$

The effective permittivity, as indicated in (21), is isotropic due to the random orientation of the scatterer species. The above result for the effective permittivity of a heterogeneous medium containing multiple species of scatterers will reduce to that of a two-phase mixing medium containing a single species of randomly oriented spheroids embedded in a background medium [*Yueh et al.*, 1990; *Nghiem et al.*, 1993a]. In the next section the effective permittivity is used in the derivation of a complete set of polarimetric backscattering coefficients under the distorted Born approximation.

3. Scattering Coefficients

For applications to polarimetric remote sensing of geophysical media, it is necessary to derive the full set of polarimetric backscattering coefficients constituting the polarimetric covariance matrix. An electromagnetic wave incident on heterogeneous media is scattered by embedded inhomogeneities which also dictates the wave propagation and attenuation characterized by the effective permittivity obtained in the last section. Thus the same physical description of the media used to calculate the effective permittivity must be used for a consistent derivation of the scattering coefficients.

Consider an electromagnetic wave impinging upon layered inhomogeneous media in the direction of wave vector $\bar{k}_{0i}$ with an incident angle of θ_{0i}, as

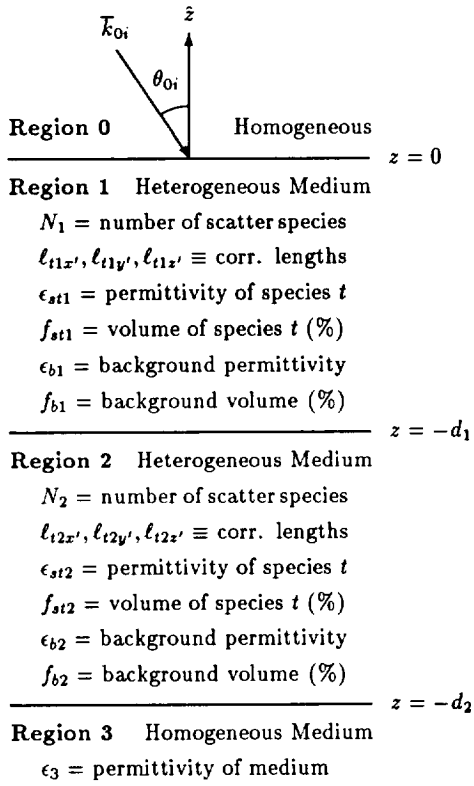

Figure 1. Inhomogeneous media with multiple species of scatterers.

shown in Figure 1. The upper half space is air and the underlying medium is homogeneous. Each region in the layered configuration is inhomogeneous and contains multiple species of scatterers which are ellipsoidal and randomly oriented. Polarimetric scattering coefficients of the layered media are defined with ensemble averages of scattered fields with all polarization combinations. These averages are calculated with spatial integrations over products of dyadic Green's function G (DGFs), mean field F, and correlation function C as follows

$$\langle \bar{E}_{0s}(\bar{r}) \cdot \bar{E}^*_{0s}(\bar{r}) \rangle = \sum_{n=1}^{2} \sum_{t=1}^{N_n} \sum_{i,j,k,l,m}^{x,y,z} k_0^4 \int_0^{2\pi} d\gamma \int_0^{\pi} d\beta \int_0^{2\pi} d\alpha$$

$$\cdot \int_{V_n} d\bar{r}_n \int_{V_n} d\bar{r}_n^o \, p_n(\alpha, \beta, \gamma) C_{t\xi njklm}(\bar{r}_n, \bar{r}_n^o; \alpha, \beta, \gamma)$$

$$\cdot [\langle G_{0nij}(\bar{r}, \bar{r}_n) \rangle \langle F_{nk}(\bar{r}_n) \rangle] \cdot [\langle G_{0nil}(\bar{r}, \bar{r}_n^o) \rangle \langle F_{nm}(\bar{r}_n^o) \rangle]^* \quad (22)$$

where t stands for the scatterer species t, and N_n is the number of species in region $n = 1, 2$. The DGFs and the mean fields are given by *Nghiem et al.* [1990].

Physical properties of the scatterers are characterized by correlation function C defined in the spatial and spectral domains as

$$C_{t\xi njklm}(\bar{r}_n, \bar{r}_n^o; \alpha, \beta, \gamma)$$

$$= \langle \xi_{tnjk}(\bar{r}_n) \xi^*_{tnlm}(\bar{r}_n^o) | \alpha(\bar{r}_n), \beta(\bar{r}_n), \gamma(\bar{r}_n) \rangle \quad (23a)$$

$$C_{t\xi njklm}(\bar{r}_n, \bar{r}_n^o; \alpha, \beta, \gamma)$$

$$= \int_{-\infty}^{\infty} d\bar{\beta} \, \Phi_{tnjklm}(\bar{\beta}) e^{-i\bar{\beta} \cdot (\bar{r}_n - \bar{r}_n^o)} \qquad n = 1, 2 \quad (23b)$$

which are expressed in the global coordinate system $(\hat{x}, \hat{y}, \hat{z})$ and related by the rotation transformation with Eulerian angles (α, β, γ) to those in the local coordinate system $(\hat{x}', \hat{y}', \hat{z}')$. Function Φ_{tnjklm} is a product of variance Γ_{tnjklm} and normalized functional part $\Phi_{t\xi n}$

$$\Phi_{tnjklm}(\bar{\beta}) = \Gamma_{tnjklm} \Phi_{t\xi n}(\bar{\beta}) \quad (24)$$

where $\Phi_{t\xi n}$ is defined in the same manner as in (3) for ellipsoidal scatterers with $\ell_{ix'}$, $\ell_{iy'}$, and $\ell_{iz'}$ replaced by $\ell_{tnx'}$, $\ell_{tny'}$, and $\ell_{tnz'}$ for species t in region n.

Variance Γ_{tnjklm} is related to local principal variance $\delta_{tnj'k'}$ which is defined as in (4) but the last term in the product is complex conjugated

$$\delta_{tnj'k'} = \delta^*_{tnk'j'} = f_{stn} f_{bn} (\xi_{tnj'} - \xi_{bnj'})(\xi_{tnk'} - \xi_{bnk'})^* \quad (25)$$

Note that all quantities in the right-hand side of (25) is the same as in the calculation of the effective permittivity; here subscript t (instead of i as in (4)) is used to denote the species and subscript n is for region n as indicated earlier. For ξ's in (25), (5) is used with subscript i replaced by tn, ϵ_{tn} for the scatterers, ϵ_{bn} for the background, and ϵ_{gn} for the auxiliary permittivity in region n. After the Eulerian transformations into the global coordinates, element Γ_{tnjklm} in the fourth-rank variance tensor $\bar{\bar{\Gamma}}_{tn}$ becomes

$$\Gamma_{tnjklm} = \sum_{u,v}^{x,y,z} \delta_{tnuv} a_{ujk} a_{vlm} = \delta_{tnx'x'} a_{xjk} a_{xlm}$$

$$+ \delta_{tnx'y'} a_{xjk} a_{ylm} + \delta_{tnx'z'} a_{xjk} a_{zlm} + \delta_{tny'x'} a_{yjk} a_{xlm}$$

$$+ \delta_{tny'y'} a_{yjk} a_{ylm} + \delta_{tny'z'} a_{yjk} a_{zlm} + \delta_{tnz'x'} a_{zjk} a_{xlm}$$

$$+ \delta_{tnz'y'} a_{zjk} a_{ylm} + \delta_{tnz'z'} a_{zjk} a_{zlm} \quad (26)$$

When integrations over Eulerian angles of the probability density function (8) for random orientations are applied to the variances in (26), the averaged variance is defined, for latter consideration, as

$$\Delta_{tnjklm} = \sum_{u,v}^{x,y,z} \int_0^{2\pi} d\gamma \int_0^{\pi} d\beta \int_0^{2\pi} d\alpha \cdot p_n(\alpha, \beta, \gamma)\delta_{tnuv}a_{ujk}a_{vlm} \tag{27}$$

Each of the six subscripts u, j, k, v, l, or m has three components x, y, and z; thus there are 3^6 or 729 terms to be integrated over the Eulerian angles in (27), and among those, 540 integrations turn out to be zero. The nonzero results are presented in Appendix C.

With the above correlation functions, correlations of the scattered fields can now be determined by (22) to obtain polarimetric scattering coefficients defined by [*Nghiem et al.*, 1990]

$$\sigma_{\mu\tau\nu\kappa} = \lim_{\substack{r\to\infty \\ A\to\infty}} \frac{4\pi r^2}{A} \frac{\langle E_{\mu s}E^*_{\nu s}\rangle}{E_{\tau o}E^*_{\kappa o}} \tag{28}$$

where subscript o denotes incident fields and s for scattered fields, subscripts μ, ν, τ, or κ can be horizontal (h) or vertical (v) polarization, r is the range from the antenna to the target, and A is the illuminated area. Conventional backscattering coefficients are $\sigma_{hh} \equiv \sigma_{hhhh}$, $\sigma_{vv} \equiv \sigma_{vvvv}$, and $\sigma_{hv} \equiv \sigma_{hvhv}$. Backscatter ratios are defined as $\gamma = \sigma_{vv}/\sigma_{hh}$ and $e = \sigma_{hv}/\sigma_{hh}$. Correlation coefficient ρ between the horizontal and vertical returns is $\rho = \sigma_{hhvv}/(\sigma_{hhhh}\sigma_{vvvv})^{1/2}$.

All integrations in (22) are carried out analytically except the triple integration over the Eulerian angles which may be intensive in computer time for numerical solution. Under the low-frequency approximation, an analytical solution, which is computationally efficient, is obtained and the result is expressed as

$$\sigma_{\mu\tau\nu\kappa} = \pi k_0^4 \sum_{t=1}^{N_1} \sum_{a,b,c,d}^{-1,1} \sum_{j,k,l,m}^{x,y,z} \Psi^{ab}_{1\mu\tau jk}\Psi^{cd*}_{1\nu\kappa lm} W^{abcd}_{t1jklm} + \pi k_0^4 \sum_{t=1}^{N_2} \sum_{p,q,r,s}^{d,u} \sum_{j,k,l,m}^{x,y,z} \Psi^{pq}_{2\mu\tau jk}\Psi^{rs*}_{2\nu\kappa lm} W^{pqrs}_{t2jklm} \tag{29}$$

in which -1 or d is for downgoing waves and 1 or u for upgoing waves. Expressions for Ψ's have been derived by *Nghiem et al.* [1990]. Quantity W^{abcd}_{t1jklm} for region 1 in (29) is

$$W^{abcd}_{t1jklm} = \int_0^{2\pi} d\gamma \int_0^{\pi} d\beta \int_0^{2\pi} d\alpha\, p(\alpha, \beta, \gamma)\Gamma_{t1jklm}I^{abcd}_{t1} \tag{30}$$

where I^{abcd}_{t1} is the integral of the correlation function and the phase in region 1 over the z component of the spectral domain and thickness d_1; the integral is carried out under the low-frequency condition as

$$I^{abcd}_{t1} = \int_{-\infty}^{\infty} d\beta_z\, \Phi_{t1\xi}(2\bar{k}_{pi}, \beta_z) \int_{-d_1}^{0} dz_1\, e^{-i(\beta_z - \kappa_{ab})z_1} \cdot \int_{-d_1}^{0} dz_1^o\, e^{i(\beta_z - \kappa_{cd})z_1^o} \approx 2\pi i\Phi_{t1\xi}(0)\left[\frac{e^{-i(\kappa_{ab}-\kappa_{cd})d_1} - 1}{\kappa_{ab} - \kappa_{cd}}\right] \tag{31}$$

With (26), (27), and (30) W^{abcd}_{t1jklm} is arranged in the following simple form:

$$W^{abcd}_{t1jklm} = \Delta_{t1jklm}I^{abcd}_{t1} \tag{32}$$

Similarly, quantity W^{pqrs}_{t2jklm} for region 2 in (29) is

$$W^{pqrs}_{t2jklm} = \int_0^{2\pi} d\gamma \int_0^{\pi} d\beta \int_0^{2\pi} d\alpha\, p(\alpha, \beta, \gamma)\Gamma_{t2jklm}I^{pqrs}_{t2} \tag{33}$$

where the integral of I^{pqrs}_{t2} is carried out under the low-frequency approximation for thickness $(d_2 - d_1)$ of region 2 as

$$I^{pqrs}_{t2} = \int_{-\infty}^{\infty} d\beta_z\, \Phi_{t2\xi}(2\bar{k}_{pi}, \beta_z) \int_{-d_2}^{-d_1} dz_2\, e^{-i(\beta_z - \kappa_{pq})z_2} \cdot \int_{-d_2}^{-d_1} dz_2^o\, e^{i(\beta_z - \kappa_{rs})z_2^o} = 2\pi i\Phi_{t2\xi}(0)\left[\frac{e^{-i(\kappa_{pq}-\kappa_{rs})d_2} - e^{-i(\kappa_{pq}-\kappa_{rs})d_1}}{\kappa_{pq} - \kappa_{rs}}\right] \tag{34}$$

From the results in (26), (27), and (33), it is observed that W^{pqrs}_{t2jklm} is simply

$$W^{pqrs}_{t2jklm} = \Delta_{t2jklm}I^{pqrs}_{t2} \tag{35}$$

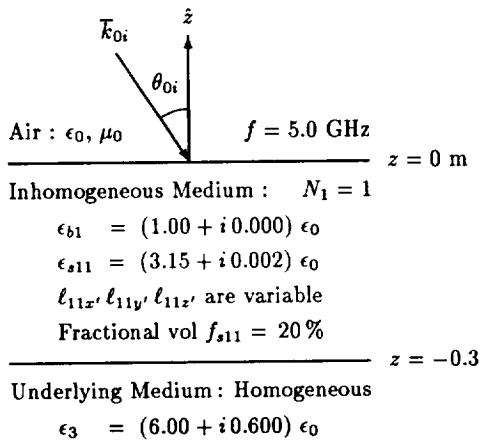

Figure 2. Parameters to study effects of scatterer shapes.

Note that the above results for the polarimetric scattering coefficients are expressed in the scattered basis. Both scattering regions in this configuration contain multiple species of ellipsoidal shapes, and the scattering media are effectively isotropic due to the random orientation. For a simpler configuration such as a half space or a scattering layer over a half space, the results are applicable by just setting the appropriate thicknesses. In the next section the model is applied to study the polarimetric scattering properties from heterogeneous media.

4. Results

4.1. Effects of Scatterer Shapes

In natural media the shape of scatterers such as ice grains in snow is particularly subjected to temperature, medium metamorphoses, or environmental variations. The model in this paper accounts for various shapes which can be spherical, prolate or oblate spheroidal, or ellipsoidal in general. For an inhomogeneous medium with a fixed number of scatterers and fractional volume, the shape of the scatterers is a significant factor on the effective permittivity and the scattering coefficients of the medium. To study effects of the scatterer shape, consider a layered medium such as that described in Figure 2. The scattering region consists of an air background and embedded scatterers of 20% fractional volume and permittivity $(3.15 + i0.002)\epsilon_0$ for ice at the C band frequency of $f = 5$ GHz. The underlying medium has a permittivity of $(6.0 + i0.6)\epsilon_0$, which is in the permittivity range for soil.

Table 1. Correlation Lengths and Effective Permittivities

Shape	$\ell_{1x'}$, mm	$\ell_{1y'}$, mm	$\ell_{1z'}$, mm	$\epsilon_{eff1}/\epsilon_0$
Spherical	0.15	0.15	0.15	$1.29 + i1.95 \times 10^{-4}$
Prolate	0.05	0.05	1.35	$1.31 + i2.27 \times 10^{-4}$
Oblate	0.58	0.58	0.01	$1.33 + i2.63 \times 10^{-4}$
Ellipsoidal	1.35	0.25	0.01	$1.32 + i2.64 \times 10^{-4}$

Four different shapes of scatterers are investigated: spherical, prolate spheroidal, oblate spheroidal, and ellipsoidal. The fractional volume and the number of scatterers are kept the same in all cases, and the nonspherical scatterers are randomly oriented. For the ellipsoidal shape the longest correlation length is taken to be equal to that of the prolate spheroidal shape, the shortest correlation length is the same as that of the oblate spheroid, and the meridian correlation is chosen by setting the surface area (defined by the two longer correlation lengths) identical to that of the oblate spheroid. Correlation lengths and calculated effective permittivities corresponding to the various shapes are reported in Table 1. It is seen that the effective permittivity is increasing when the scatterer shape varies from spherical, to prolate spheroidal, and then to oblate spheroidal forms. Permittivity results for the ellipsoids and oblate spheroids are similar due to the similar cross sections of the scatterers in the two cases.

Differences in the scatterer shape are also manifested in scattering coefficients. Copolarized backscattering coefficients for different scatterer shapes are shown in Figure 3. Oscillations in the curves of the scattering coefficients are due to multiple interactions with the layer boundaries. The copolarized backscattering increases as the scatterer cross section increases from the spherical to prolate, and then to oblate spheroidal form. The copolarization results for the ellipsoidal and the oblate spheroidal forms are similar. For cross-polarized returns, the spherical case gives zero value under the first-order distorted Born approximation. Cross-polarized backscattering coefficients for nonspherical scatterers are plotted as a function of incident angles in Figure 4. The oblate spheroids provide the highest returns while the ellipsoids and the prolate spheroids have a similar cross-polarization effect due to the same size in their longest correlation lengths. As illustrated, the ellipsoids behave as a hybrid between the oblate and the prolate spheroids.

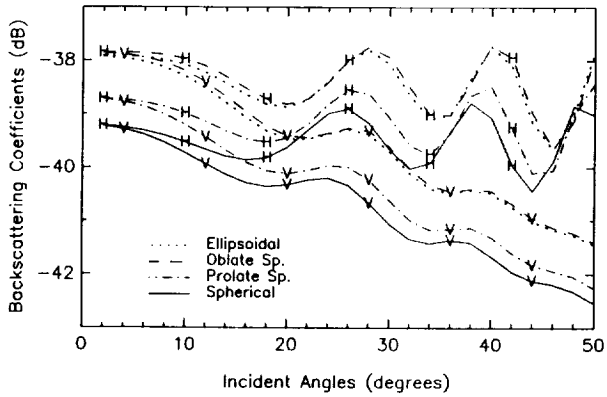

Figure 3. Copolarized backscattering coefficients $H = \sigma_{hh}$ and $V = \sigma_{vv}$ for different scatterer shapes.

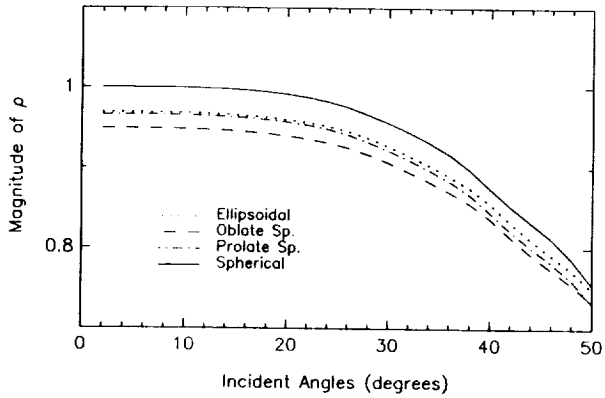

Figure 5. Magnitudes of correlation coefficient ρ for different scatterer shapes.

A common feature in all of the cases for the different shapes is the effective isotropy of the inhomogeneous medium. For the case of nonspherical scatterers the medium is rendered isotropic by random scatterer orientations with no preferred direction. Wave speed and attenuation in the inhomogeneous isotropic medium is the same for horizontal and vertical waves. This results in correlation coefficient ρ between h and v waves with a small phase. Magnitudes of ρ plotted in Figure 5 show a similar variation as a function of incident angles for the different shapes of the scatterers with a stronger decorrelation effect from nonspherical scatterers.

4.2. Effects of Multiple Species

The multispecies model in this paper allows the coexistence of disclike and needlelike scatterers.

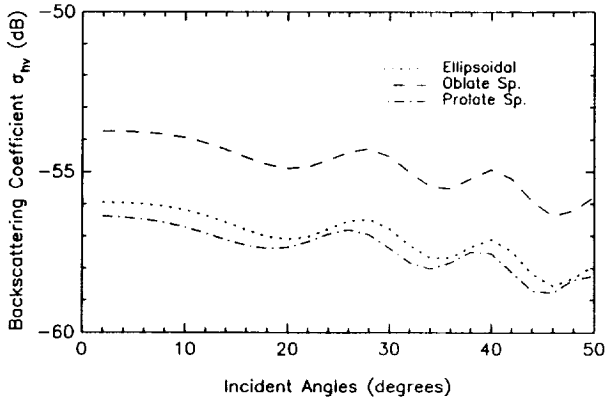

Figure 4. Cross-polarized backscattering coefficients for different scatterer shapes.

Effects of multiple species are studied with the configuration described in Figure 6, which corresponds to a soybean canopy [*Nghiem et al.*, 1993a, case 9-03-86] where the canopy was modeled with only disclike scatterers. The soil surface is rough and all input parameters are given by *Nghiem et al.* [1993a].

Now, needlelike scatterers are introduced into the canopy by allocating part of the total scatterer fractional volume to the new scatterer species whose permittivity is taken to be the same as that of the disclike scatterers. The needlelike form is depicted by a prolate spheroidal shape with correlation lengths of 0.3 mm and 5.0 mm. Note that the

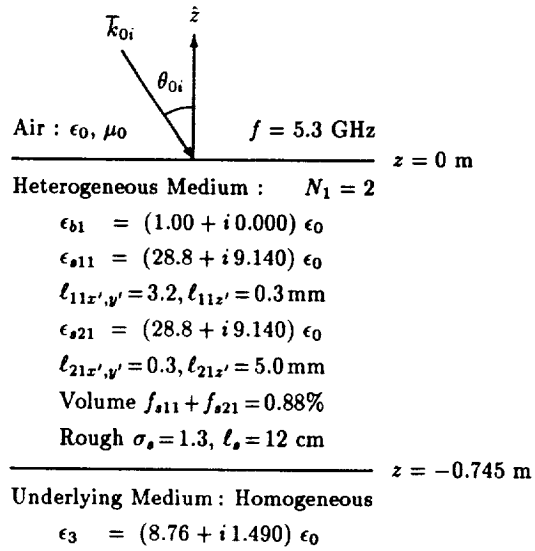

Figure 6. Parameters to study effects of multiple species.

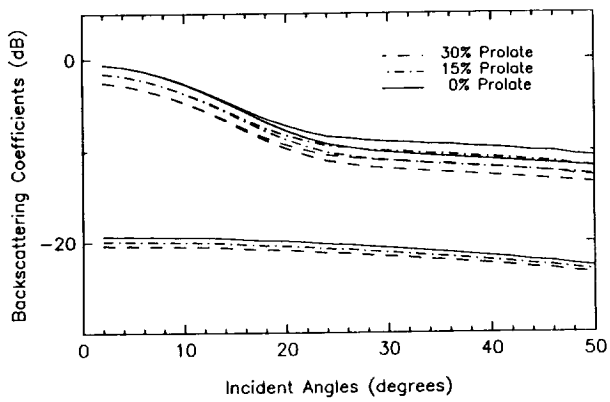

Figure 7. Backscattering coefficients for different mixtures of multiple species. For each mixture the top curve is for σ_{hh}, the middle for σ_{vv}, and the bottom for σ_{hv}.

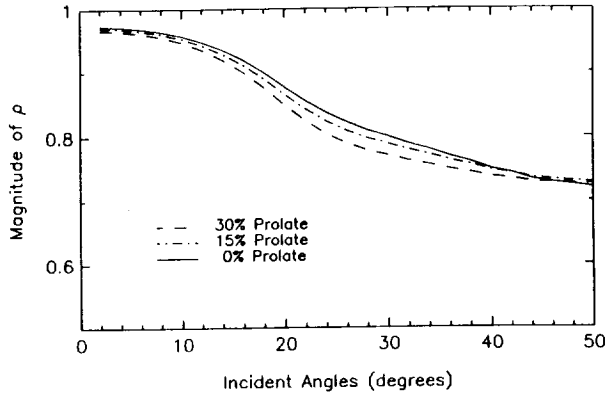

Figure 8. Magnitudes of correlation coefficient ρ for different mixtures of multiple species.

volume of an individual needlelike scatterer is much smaller than that of the disclike scatterer for the given parameters. Three cases are considered here: Case 1 has 100% oblate spheroids, case 2 has 85% oblate and 15% prolate, and case 3 has 70% oblate and 30% prolate spheroids.

Backscattering coefficients decrease, as seen in Figure 7, for increasing needlelike species, which has a smaller total cross section. Figure 7 also shows that the decrease in the copolarized returns is more than that in the cross-polarized return. Again due to the effective isotropy, the phase of correlation coefficient ρ is small for the cases under consideration. While the magnitude of ρ for different mixtures is similar as indicated in Figure 8, intensity ratio $e = \sigma_{hv}/\sigma_{hh}$ is higher for a mixture containing more needlelike scatterers, as shown in Figure 9. This will result in a copolarized signature with a higher pedestal [*Nghiem et al.*, 1990] indicating a stronger depolarization effect.

4.3. Applications

This section presents applications of the multispecies model to study polarimetric scattering signatures from inhomogeneous media. A very lossy species of scatterers with a high permittivity strongly affects wave propagation, attenuation, and scattering in a multispecies medium. This model includes such a species together with other scattering species to investigate effects of moisture in a scattering medium such as polar ice sheets. Effects of frost flowers on thin saline ice are also studied with multispecies mixtures of fanlike ice crystals and brine inclusions.

Temperature changes cause variations in moisture content of snowpack such as polar ice sheets, which are important to global climate because of their vast coverage [*Thomas et al.*, 1985]. It has been observed that σ_{hh} is sensitive to snow moisture and generally decreases with snow wetness [*Stiles and Ulaby*, 1980]. The configuration in Figure 10 is a half space consisting of an air background and two species of spherical scatterers: one with fractional volume of 0.3 and a relative permittivity of $3.15 + i0.0012$ for ice grains, the other with variable fractional volume and a relative permittivity of $65 + i34$ for water. Correlation lengths are determined from scatterer sizes [*Yueh et al.*, 1990]. Backscattering coefficient σ_{vv} at 5.3 GHz and a 20° incident angle, corresponding to the operating parameters of ERS 1 SAR (the first European Remote

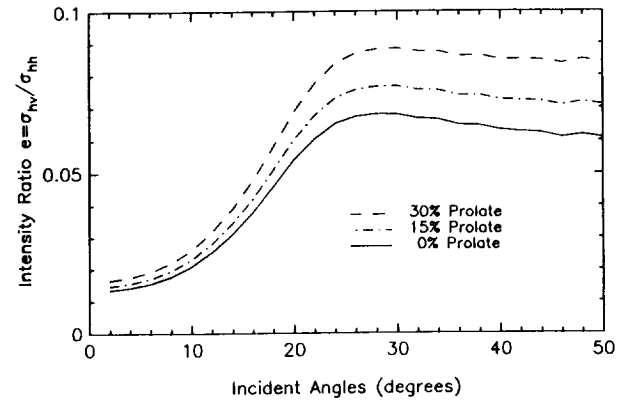

Figure 9. Intensity ratio $e = \sigma_{hv}/\sigma_{hh}$ for different mixtures of multiple species.

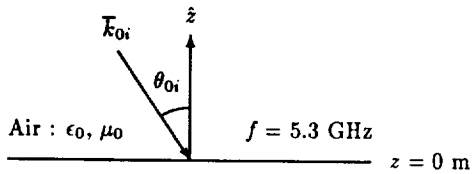

Heterogeneous Medium : $N_1 = 2$

$\epsilon_{b1} = (1.00 + i\,0.000)\,\epsilon_0$

$\epsilon_{s11} = (3.15 + i\,.0012)\,\epsilon_0$

$\ell_{11x'} = \ell_{11y'} = \ell_{11z'}$ = vary

Fractional vol f_{s11} = 30%

$\epsilon_{s21} = (65.0 + i\,34.00)\,\epsilon_0$

$\ell_{21x'} = \ell_{21y'} = \ell_{21z'} = .11$mm

Fractional vol f_{s21} = vary

Figure 10. Parameters of a half-space multispecies model for dry and wet snowpack.

Sensing synthetic aperture radar), is plotted as a function of ice grain size for various moisture contents from dry to wet conditions in Figure 11. In addition to the inverse relation between σ_{vv} and the moisture with a good sensitivity, the results show that the change in backscatter is larger for drier conditions and smaller grains, and ice grain size is important to the backscatter.

Leads in the Arctic ice pack are important to heat exchange with the atmosphere and salt flux into the upper ocean [*Maykut*, 1982]. Surface characteristics of thin sea ice in leads are dominated by the formation of frost flowers with a high salinity [*Perovich and Richter-Menge*, 1994]. This layer is simulated with a mixture containing randomly oriented ellipsoids and brine infiltration by a volume ratio of three parts ice

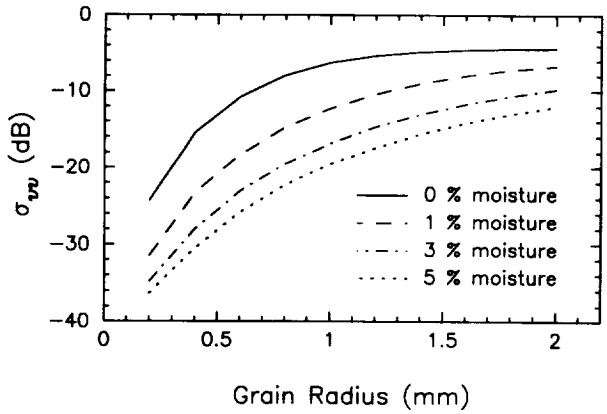

Figure 11. Backscattering coefficient σ_{vv} as a function of grain size for various moisture contents.

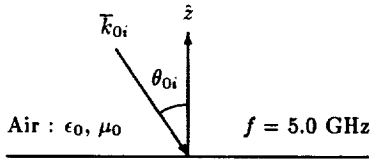

Heterogeneous Medium : $N_1 = 2$

$\epsilon_{b1} = (1.00 + i\,0.000)\,\epsilon_0$

$\epsilon_{s11} = (52.5 + i\,44.07)\,\epsilon_0$

$\ell_{11x'} = \ell_{11y'} = \ell_{11z'} = .5$mm

Fractional vol f_{s11} = 2.0%

$\epsilon_{s21} = (3.19 + i\,.0014)\,\epsilon_0$

$30\ell_{21x'}, 1.5\ell_{21y'}, \ell_{21z'} = 3$mm

Fractional vol f_{s21} = 6.0%

Rough $\sigma_s = 1.0$, $\ell_s = 10$mm

z = −0.025 m

Inhomogeneous Medium : $N_2 = 1$

$\epsilon_{b2} = (3.19 + i\,.0014)\,\epsilon_0$

$\epsilon_{s12} = (52.5 + i\,44.07)\,\epsilon_0$

Cor length $\ell_{12x'} = .236$mm

Cor length $\ell_{12y'} = .660$mm

Cor length $\ell_{12z'} = .792$mm

Fractional vol f_{s12} = 10.4%

z = −0.137 m

Underlying Medium : Homogeneous

$\epsilon_3 = (60.7 + i\,40.70)\,\epsilon_0$

Figure 12. Parameters of a layered multispecies model for frost-covered saline ice.

and one part brine [*Perovich and Richter-Menge*, 1994]. The ice crystals are characterized with correlation lengths $\ell_{11x'}$ = 0.1 mm, $\ell_{11y'}$ = 2 mm, and $\ell_{11z'}$ = 3 mm to describe the fanlike form. Covered under the multispecies medium is an anisotropic layer of saline ice composed of ellipsoidal brine inclusions preferentially oriented in the vertical direction in an ice background [*Nghiem et al.*, 1993b]. The inhomogeneities in the ice layer are dominated by brine inclusions and this layer is modeled with a single scattering species. Model characterization parameters are given in Figure 12 for the layered media. Figure 13 compares polarimetric backscattering results calculated from the model with measured data obtained by the Jet Propulsion Laboratory polarimetric scatterometer at C band (center frequency at 5 GHz) during the Cold Regions Research and Engineering Laboratory Experiment in 1993 (CRRELEX 1993) [*Nghiem et al.*, 1994] for thin bare saline ice. The curves calculated from bare the model compare well with the measured

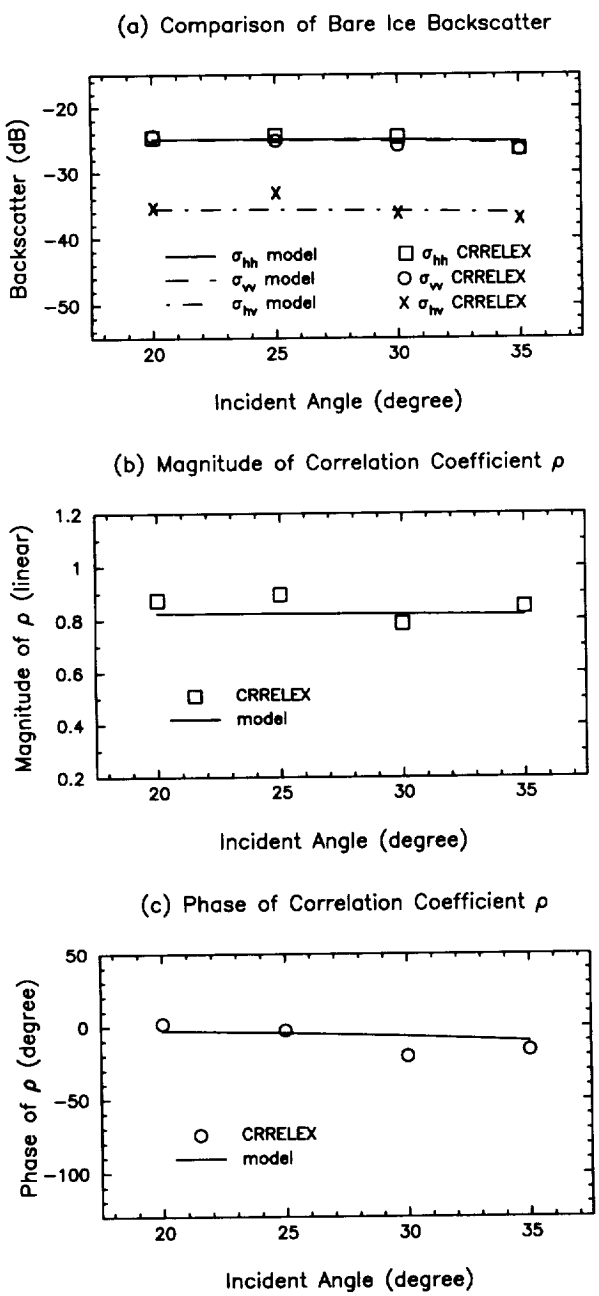

Figure 13. Polarimetric scattering results for bare saline ice: squares, circles, and crosses are for measured data from the 1993 Cold Regions Research and Engineering Laboratory Experiment (CRRELEX); curves are model results.

data. These curves are for the layered medium with a smooth surface and without the covering layer, which correspond to the configuration of the bare saline ice for the CRRELEX 1993 measurements.

Then, the covering layer is included in the model to simulate a full areal coverage of the frost flower formation. Note that the interface between this formation and the saline ice has some roughness described by a height standard deviation of σ_s = 1 mm and a surface correlation length of ℓ_s = 1 cm. The small-scale roughness on the surface is suggested by *Perovich and Richter-Menge* [1994] to serve as nucleation sites for the frost flowers. Polarimetric scattering from the surface roughness is calculated with the small perturbation method and included in the total polarimetric signatures [*Nghiem et al.*, 1993b]. The curves in Figure 14a indicate that this covering layer can increase copolarized backscattering coefficients by several decibels while there is a small effect on the cross-polarized return. Figures 14b and 14c show that the complex correlation coefficient ρ has a magnitude closer to 1 and a smaller phase; this behavior is more similar to the isotropic scattering characteristics. This is caused by the random orientation of the ellipsoids in the covering layer and the nondirectional feature of the surface roughness. Figure 15 presents the normalized polarization signatures σ_n at incident angle θ_{0i} = 35° as a function of orientation angle α_c and ellipticity angle β_c [*Nghiem et al.*, 1990] for CRRELEX-observed (Figure 15a) and calculated (Figure 15b) bare saline ice. The signatures of bare ice from CRRELEX data and model calculation compare well. The signature of the covered layered medium in Figure 16 (also at 35° incident angle) has a maximum in the middle (α_c = 90° and β_c = 0°) and a lower pedestal corresponding to a weaker depolarization effect [*Nghiem et al.*, 1990]. Parameters in covariance matrices corresponding to the above polarization signatures are listed in Table 2, which shows a good match of all covariance parameters for experimental and theoretical results of bare saline ice.

5. Summary

This paper presents a model for layered inhomogeneous media containing multiple species of scatterers to calculate polarimetric backscattering signatures. The species are allowed to have different size, shape, and permittivity. The strong permittivity fluctuation theory is extended to account for the multispecies in the derivation of the effective permittivity with a random distribution of orientations characterized with Eulerian rotation angles.

Polarimetric backscattering coefficients are ob-

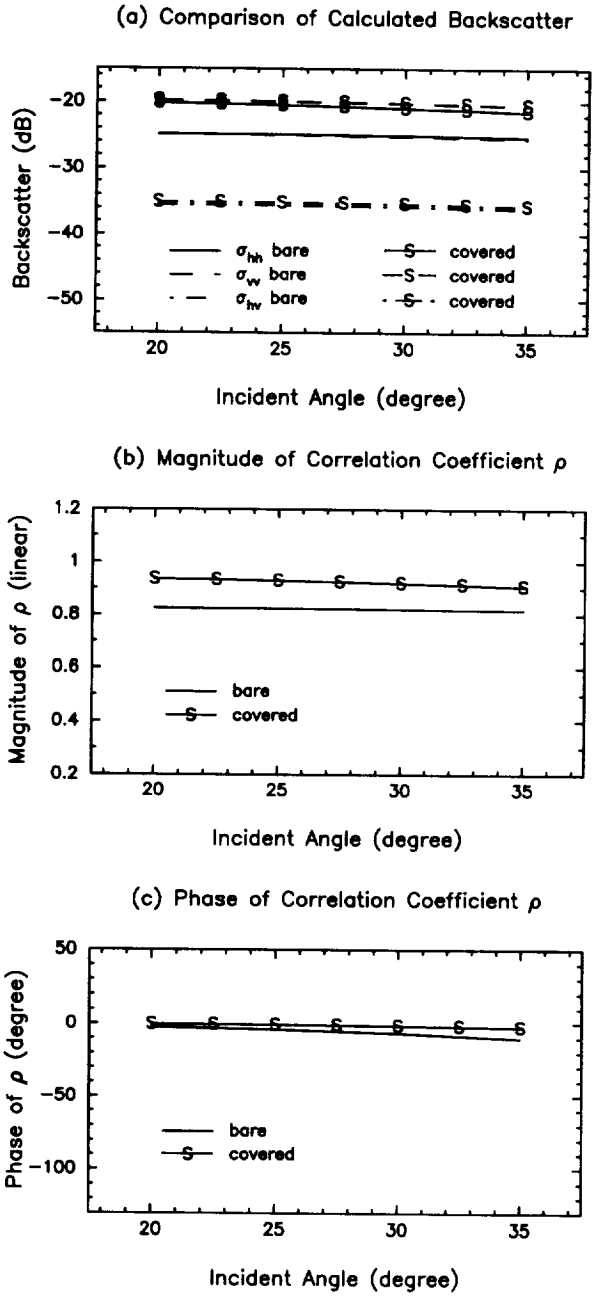

Figure 14. Polarimetric scattering results for bare and frost-covered saline ice: curves without the symbol "S" are model results for bare saline ice, and those with the symbol "S" are model results for frost-covered saline ice.

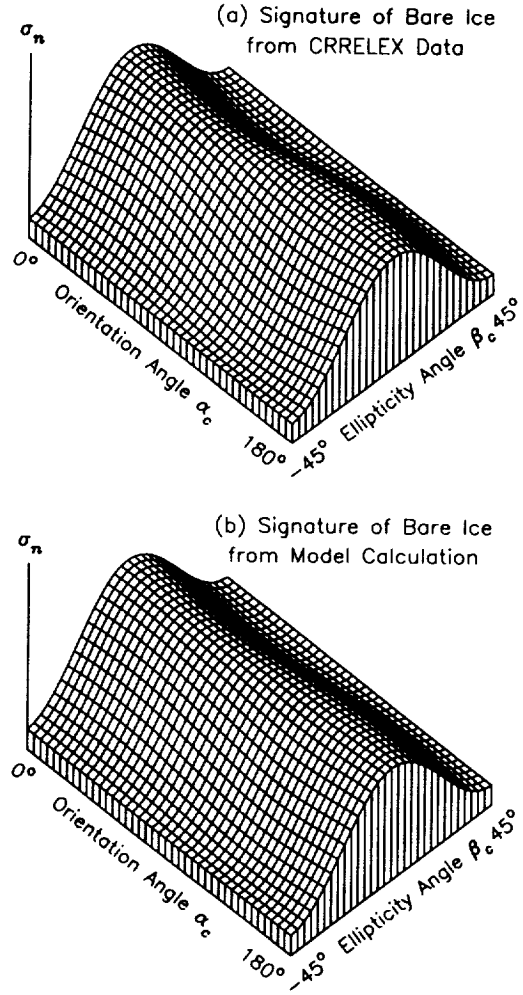

Figure 15. Normalized copolarized polarimetric signatures at incident angle $\theta_{0i} = 35°$ of (a) bare saline ice from CRRELEX 1993 data and (b) bare saline ice from model calculation.

tained consistently with the same physical description used in the effective permittivity calculation. Under the first-order distorted Born approximation, results for the scattering coefficients contain triple integrations over Eulerian angles, which can be carried out numerically. Analytical results are also obtained under the low-frequency approximation involving 729 terms for the random orientation distribution. The model indicates that nonspherical scatterers with larger cross sections give higher effective permittivity and stronger scattering effects. The random orientation renders the medium isotropic for all scatterer shapes; however, the shapes of the scatterers are important to cross-polarized returns and magnitudes of polarimetric correlation coefficient ρ. For a mixture of oblate (disclike) and prolate (needlelike) spheroids the oblate species contributes more to the total back-

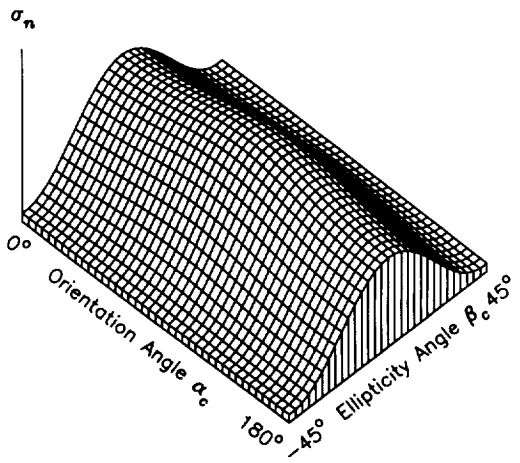

Figure 16. Normalized copolarized polarimetric signatures at incident angle $\theta_{0i} = 35°$ of frost-covered saline ice from model simulation.

scatter, and the prolate species increases the cross-polarized intensity ratio $e = \sigma_{hv}/\sigma_{hh}$.

The multispecies model allows the inclusion of moisture in a scattering medium. Besides a high sensitivity of backscatter to moisture content in snowpack as observed by *Stiles and Ulaby* [1980], results for backscattering coefficients with vertical polarization at C band (ERS 1 polarization and frequency) indicate a stronger dependence to the moisture for drier and finer snow and ice grain size is important to the backscatter. Effects of a multispecies covering layer such as frost-covered saline ice are also studied. Theoretical results for bare saline compare well with measured data at 5 GHz from CRRELEX 1993. Then, the model is used to simulate a full areal coverage of frost formation with a layer of fanlike crystals including brine infiltration. The results reveal that the frost cover with a rough interface can significantly increase the backscatter from thin saline ice and the polarimetric signature becomes closer to the isotropic characteristics. The strong effects of frost flower formation suggest that an experiment needs to be conducted to study in detail their impact on polarization signatures of young sea ice and to provide good coordinated backscatter and ice characterization data for a better direction and substantiation of the sea ice modeling.

Table 2. Parameters at $\theta_{0i} = 35°$ in Covariance Matrices of Bare and Covered Saline Ice

Case	σ_{hh}, dB	γ, dB	e, dB	$\lvert\rho\rvert$	$\angle\rho$, deg
Bare ice (CRRELEX 1993)	−26.3	−0.2	−10.8	0.85	−16.3
Bare ice (Model result)	−25.2	−0.2	−10.9	0.82	−10.2
Covered ice (Simulation)	−21.4	+0.9	−14.3	0.91	−2.8

CRRELEX 1993, Cold Regions Research and Engineering Laboratory Experiment in 1993.

With the consideration of multiple species the model advances toward a better representation of geophysical media. However, the model needs further development to cope with the complexity of natural geophysical media. For instance, particles are coated due to disseminated sulphide mineralization [*Wait*, 1989]. Ice grains in snow are distributed in size, metamorphosed, and clustered [*Colbeck*, 1986, 1987]; anisotropy in snow was also quantified [*Davis and Dozier*, 1989]. Columnar sea ice is an anisotropic multispecies medium containing air and brine inclusions, whose phase distributions are thermodynamically dependent [*Weeks and Ackley*, 1982] and influenced by environmental effects such as temperature variations [*Arcone et al.*, 1986].

Appendix A: Eulerian Rotations Between Local and Global Coordinates

To relate the local scatterer coordinate system (x', y', z') to the global coordinate system (x, y, z), Eulerian angles α, β, and γ are used as illustrated in Figure A1.

The rotation $\alpha(0 < \alpha < 2\pi)$ about the z' axis, $\beta(0 < \beta < \pi)$ about the y_1 axis, and $\gamma(0 < \gamma < 2\pi)$ about the z_2 axis are described with the following relations:

$$\begin{bmatrix} x_1 \\ y_1 \\ z_1 \end{bmatrix} = \bar{\bar{T}}_\alpha \cdot \begin{bmatrix} x' \\ y' \\ z' \end{bmatrix} = \begin{bmatrix} \cos\alpha & \sin\alpha & 0 \\ -\sin\alpha & \cos\alpha & 0 \\ 0 & 0 & 1 \end{bmatrix} \cdot \begin{bmatrix} x' \\ y' \\ z' \end{bmatrix} \tag{A1a}$$

$$\begin{bmatrix} x_2 \\ y_2 \\ z_2 \end{bmatrix} = \bar{\bar{T}}_\beta \cdot \begin{bmatrix} x_1 \\ y_1 \\ z_1 \end{bmatrix} = \begin{bmatrix} \cos\beta & 0 & -\sin\beta \\ 0 & 1 & 0 \\ -\sin\beta & 0 & \cos\beta \end{bmatrix} \cdot \begin{bmatrix} x_1 \\ y_1 \\ z_1 \end{bmatrix} \tag{A1b}$$

$$\begin{bmatrix} x \\ y \\ z \end{bmatrix} = \bar{\bar{T}}_\gamma \cdot \begin{bmatrix} x_2 \\ y_2 \\ z_2 \end{bmatrix} = \begin{bmatrix} \cos\gamma & \sin\gamma & 0 \\ -\sin\gamma & \cos\gamma & 0 \\ 0 & 0 & 1 \end{bmatrix} \cdot \begin{bmatrix} x_2 \\ y_2 \\ z_2 \end{bmatrix} \tag{A1c}$$

and the resultant Eulerian transformation which rotates the global to the local scatterer coordinates is

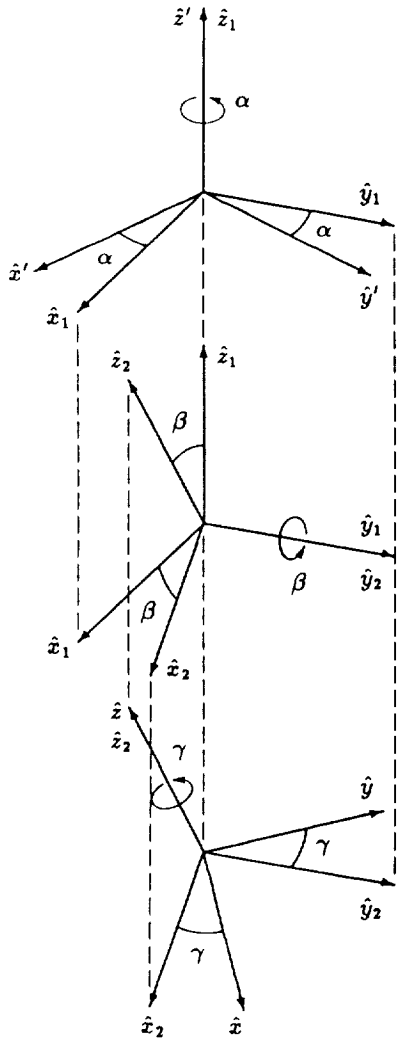

(a)

$$\overline{\overline{T}}_\alpha = \begin{bmatrix} \cos\alpha & \sin\alpha & 0 \\ -\sin\alpha & \cos\alpha & 0 \\ 0 & 0 & 1 \end{bmatrix}$$

(b)

$$\overline{\overline{T}}_\beta = \begin{bmatrix} \cos\beta & 0 & -\sin\beta \\ 0 & 1 & 0 \\ \sin\beta & 0 & \cos\beta \end{bmatrix}$$

(c)

$$\overline{\overline{T}}_\gamma = \begin{bmatrix} \cos\gamma & \sin\gamma & 0 \\ -\sin\gamma & \cos\gamma & 0 \\ 0 & 0 & 1 \end{bmatrix}$$

Figure A1. Eulerian angles: (a) α is the rotation angle about z' axis, (b) β is the rotation angle about y_1 axis, and (c) γ is the rotation angle about z_2 axis.

$$\begin{bmatrix} x' \\ y' \\ z' \end{bmatrix} = \bar{\bar{T}} \cdot \begin{bmatrix} x \\ y \\ z \end{bmatrix} = [\bar{\bar{T}}_\gamma \cdot \bar{\bar{T}}_\beta \cdot \bar{\bar{T}}_\alpha]^{-1} \cdot \begin{bmatrix} x \\ y \\ z \end{bmatrix}$$

$$= \begin{bmatrix} \cos\gamma\cos\beta\cos\alpha - \sin\gamma\sin\alpha \\ \cos\gamma\cos\beta\sin\alpha + \sin\gamma\cos\alpha \\ -\cos\gamma\sin\beta \end{bmatrix}$$

$$\begin{bmatrix} -\sin\gamma\cos\beta\cos\alpha - \cos\gamma\sin\alpha & \sin\beta\cos\alpha \\ -\sin\gamma\cos\beta\sin\alpha + \cos\gamma\cos\alpha & \sin\beta\sin\alpha \\ \sin\gamma\sin\beta & \cos\beta \end{bmatrix} \cdot \begin{bmatrix} x \\ y \\ z \end{bmatrix} \quad \text{(A2)}$$

Appendix B: Average Over Eulerian Angles

This appendix shows the average over the random orientation, described by Eulerian angles, of the product between tensor $\bar{\bar{\xi}}$ and orientation probability density function $p(\alpha, \beta, \gamma)$. The averaging integral is

$$\langle \bar{\bar{\xi}}(\bar{r}) \rangle = \int_0^{2\pi} d\gamma \int_0^{\pi} d\beta \int_0^{2\pi} d\alpha \, p(\alpha, \beta, \gamma) \bar{\bar{T}}^{-1} \cdot \bar{\bar{\xi}}(\hat{r}') \cdot \bar{\bar{T}} \quad \text{(B1)}$$

where $p(\alpha, \beta, \gamma) = \sin\beta/(8\pi^2)$ and rotation tensor $\bar{\bar{T}}$ is given by

$$\bar{\bar{T}} = \begin{bmatrix} \cos\gamma\cos\beta\cos\alpha - \sin\gamma\sin\alpha & -\sin\gamma\cos\beta\cos\alpha - \cos\gamma\sin\alpha & \sin\beta\cos\alpha \\ \cos\gamma\cos\beta\sin\alpha + \sin\gamma\cos\alpha & -\sin\gamma\cos\beta\sin\alpha + \cos\gamma\cos\alpha & \sin\beta\sin\alpha \\ -\cos\gamma\sin\beta & \sin\gamma\sin\beta & \cos\beta \end{bmatrix} \tag{B2}$$

Tensor $\bar{\bar{\xi}}(\hat{r})$ in the global coordinates (x, y, z) is obtained with the rotation operation

$$\bar{\bar{\xi}}(\hat{r}) = \bar{\bar{T}}^{-1} \cdot \bar{\bar{\xi}}(\hat{r}') \cdot \bar{\bar{T}} = \bar{\bar{T}}^{-1} \cdot \begin{bmatrix} \xi_{x'} & 0 & 0 \\ 0 & \xi_{y'} & 0 \\ 0 & 0 & \xi_{z'} \end{bmatrix} \cdot \bar{\bar{T}}$$

$$= \begin{bmatrix} \xi_{xx} & \xi_{xy} & \xi_{xz} \\ \xi_{yx} & \xi_{yy} & \xi_{yz} \\ \xi_{zx} & \xi_{zy} & \xi_{zz} \end{bmatrix} \tag{B3}$$

Explicitly, the elements of $\bar{\bar{\xi}}(\hat{r})$ in the global coordinates are

$$\begin{aligned} \xi_{xx} &= \xi_{x'}(\cos^2\gamma\cos^2\beta\cos^2\alpha + \sin^2\gamma\sin^2\alpha \\ &\quad - 2\sin\gamma\cos\gamma\cos\beta\sin\alpha\cos\alpha) \\ &\quad + \xi_{y'}(\cos^2\gamma\cos^2\beta\sin^2\alpha + \sin^2\gamma\cos^2\alpha \\ &\quad + 2\sin\gamma\cos\gamma\cos\beta\sin\alpha\cos\alpha) \\ &\quad + \xi_{z'}(\cos^2\gamma\sin^2\beta) = \xi_{x'}a_{xxx} + \xi_{y'}a_{yxx} + \xi_{z'}a_{zxx} \end{aligned} \tag{B4a}$$

$$\begin{aligned} \xi_{xy} &= -\xi_{x'}(\sin\gamma\cos\gamma\cos^2\beta\cos^2\alpha \\ &\quad + \cos^2\gamma\cos\beta\sin\alpha\cos\alpha - \sin^2\gamma\cos\beta\sin\alpha\cos\alpha \\ &\quad - \sin\gamma\cos\gamma\sin^2\alpha) - \xi_{y'}(\sin\gamma\cos\gamma\cos^2\beta\sin^2\alpha \\ &\quad - \cos^2\gamma\cos\beta\sin\alpha\cos\alpha + \sin^2\gamma\cos\beta\sin\alpha\cos\alpha \\ &\quad - \sin\gamma\cos\gamma\cos^2\alpha) - \xi_{z'}(\sin\gamma\cos\gamma\sin^2\beta) \\ &= \xi_{x'}a_{xxy} + \xi_{y'}a_{yxy} + \xi_{z'}a_{zxy} \end{aligned} \tag{B4b}$$

$$\begin{aligned} \xi_{xz} &= \xi_{x'}(\cos\gamma\sin\beta\cos\beta\cos^2\alpha \\ &\quad - \sin\gamma\sin\beta\sin\alpha\cos\alpha) \\ &\quad + \xi_{y'}(\cos\gamma\sin\beta\cos\beta\sin^2\alpha \\ &\quad + \sin\gamma\sin\beta\sin\alpha\cos\alpha) + \xi_{z'}(-\cos\gamma\sin\beta\cos\beta) \\ &= \xi_{x'}a_{xxz} + \xi_{y'}a_{yxz} + \xi_{z'}a_{zxz} \end{aligned} \tag{B4c}$$

$$\begin{aligned} \xi_{yx} &= \xi_{x'}a_{xyx} + \xi_{y'}a_{yyx} + \xi_{z'}a_{zyx} \\ &= \xi_{x'}a_{xxy} + \xi_{y'}a_{yxy} + \xi_{z'}a_{zxy} \end{aligned} \tag{B4d}$$

$$\begin{aligned} \xi_{yy} &= \xi_{x'}(\sin^2\gamma\cos^2\beta\cos^2\alpha + \cos^2\gamma\sin^2\alpha \\ &\quad + 2\sin\gamma\cos\gamma\cos\beta\sin\alpha\cos\alpha) \\ &\quad + \xi_{y'}(\sin^2\gamma\cos^2\beta\sin^2\alpha + \cos^2\gamma\cos^2\alpha \\ &\quad - 2\sin\gamma\cos\gamma\cos\beta\sin\alpha\cos\alpha) + \xi_{z'}(\sin^2\gamma\sin^2\beta) \\ &= \xi_{x'}a_{xyy} + \xi_{y'}a_{yyy} + \xi_{z'}a_{zyy} \end{aligned} \tag{B4e}$$

$$\begin{aligned} \xi_{yz} &= -\xi_{x'}(\sin\gamma\sin\beta\cos\beta\cos^2\alpha \\ &\quad + \cos\gamma\sin\beta\sin\alpha\cos\alpha) \\ &\quad - \xi_{y'}(\sin\gamma\sin\beta\cos\beta\sin^2\alpha \\ &\quad - \cos\gamma\sin\beta\sin\alpha\cos\alpha) - \xi_{z'}(-\sin\gamma\sin\beta\cos\beta) \\ &= \xi_{x'}a_{xyz} + \xi_{y'}a_{yyz} + \xi_{z'}a_{zyz} \end{aligned} \tag{B4f}$$

$$\begin{aligned} \xi_{zx} &= \xi_{x'}a_{xzx} + \xi_{y'}a_{yzx} + \xi_{z'}a_{zzx} \\ &= \xi_{x'}a_{xxz} + \xi_{y'}a_{yxz} + \xi_{z'}a_{zxz} \end{aligned} \tag{B4g}$$

$$\begin{aligned} \xi_{zy} &= \xi_{x'}a_{xzy} + \xi_{y'}a_{yzy} + \xi_{z'}a_{zzy} \\ &= \xi_{x'}a_{xyz} + \xi_{y'}a_{yyz} + \xi_{z'}a_{zyz} \end{aligned} \tag{B4h}$$

$$\begin{aligned} \xi_{zz} &= \xi_{x'}(\sin^2\beta\cos^2\alpha) + \xi_{y'}(\sin^2\beta\sin^2\alpha) + \xi_z\cos^2\beta \\ &= \xi_{x'}a_{xzz} + \xi_{y'}a_{yzz} + \xi_{z'}a_{zzz} \end{aligned} \tag{B4i}$$

Integrating over the above elements yields

$$\langle\xi_{xx}\rangle = \int_0^{2\pi} d\gamma \int_0^{\pi} d\beta \int_0^{2\pi} d\alpha\, p(\alpha, \beta, \gamma)\xi_{xx} = \tfrac{1}{3}(\xi_{x'} + \xi_{y'} + \xi_{z'}) \tag{B5a}$$

$$\langle\xi_{yy}\rangle = \int_0^{2\pi} d\gamma \int_0^{\pi} d\beta \int_0^{2\pi} d\alpha\, p(\alpha, \beta, \gamma)\xi_{yy} = \tfrac{1}{3}(\xi_{x'} + \xi_{y'} + \xi_{z'}) \tag{B5b}$$

$$\langle\xi_{zz}\rangle = \int_0^{2\pi} d\gamma \int_0^{\pi} d\beta \int_0^{2\pi} d\alpha\, p(\alpha, \beta, \gamma)\xi_{zz} = \tfrac{1}{3}(\xi_{x'} + \xi_{y'} + \xi_{z'}) \tag{B5c}$$

$$\langle \xi_{xy} \rangle = \langle \xi_{yx} \rangle = \int_0^{2\pi} d\gamma \int_0^{\pi} d\beta \int_0^{2\pi} d\alpha \; p(\alpha, \beta, \gamma) \xi_{yx} = 0 \tag{B5d}$$

$$\langle \xi_{xz} \rangle = \langle \xi_{zx} \rangle = \int_0^{2\pi} d\gamma \int_0^{\pi} d\beta \int_0^{2\pi} d\alpha \; p(\alpha, \beta, \gamma) \xi_{zx} = 0 \tag{B5e}$$

$$\langle \xi_{yz} \rangle = \langle \xi_{zy} \rangle = \int_0^{2\pi} d\gamma \int_0^{\pi} d\beta \int_0^{2\pi} d\alpha \; p(\alpha, \beta, \gamma) \xi_{zy} = 0 \tag{B5f}$$

For generality, subscript i for the scatterer species i and b for the background are not included in the notation of $\xi_{j'}(j' = x', y', z')$ which can take on the value of $\xi_{ij'}$ for scatterer species $i = 1, 2, 3, \ldots, N$ or $\xi_{bj'}$ for the background. The above results are used to obtain (9). When ξ is replaced by S, (12) is obtained.

Appendix C: Coefficients in Variances

Polarimetric scattering coefficients derived in this paper involve the terms Δ_{tnjklm} which are integrals over the Eulerian angles of the probability density function of the random orientation and the variances in the global coordinates. Δ_{tnjklm} is considered as a variance averaged over the orientation and defined by

$$\Delta_{tnjklm} = \sum_{u,v}^{x,y,z} \int_0^{2\pi} d\gamma \int_0^{\pi} d\beta \int_0^{2\pi} d\alpha p_n(\alpha, \beta, \gamma) \delta_{tnuv} a_{ujk} a_{vlm}$$

There are six subscripts associated with coefficient a's in the above equation. Each subscript can be x, y, or z; therefore, there are $3^6 = 729$ terms in total. After being integrated, 540 terms become zero and the remaining nonzero terms are presented in this appendix. Coefficient a's, given in appendix B, come from the rotation operation on the tensors. For instance, consider the following integration of the product of the orientation probability and $a_{xxx}a_{xxx}$

$$\int_0^{2\pi} d\gamma \int_0^{\pi} d\beta \int_0^{2\pi} d\alpha \; p_n(\alpha, \beta, \gamma) a_{xxx} a_{xxx}$$

$$= \int_0^{2\pi} d\gamma \int_0^{\pi} d\beta \int_0^{2\pi} d\alpha \; \frac{\sin \beta}{8\pi^2}$$

$$\cdot [\cos^4 \gamma \cos^4 \beta \cos^4 \alpha + \sin^4 \gamma \sin^4 \alpha$$

$$+ 4 \sin^4 \gamma \cos^2 \gamma \cos^2 \beta \sin^2 \alpha \cos^2 \alpha$$

$$+ 2 \sin^2 \gamma \cos^2 \gamma \cos^2 \beta \sin^2 \alpha \cos^2 \alpha$$

$$- 4 \sin \gamma \cos^3 \gamma \cos^3 \beta \sin \alpha \cos^3 \alpha$$

$$- 4 \sin^3 \gamma \cos \gamma \cos \beta \sin^3 \alpha \cos \alpha] = 1/5$$

The results of the integrations show that many combinations of a's have one of the values: 1/5, 2/15, 1/15, or $-1/30$. Actually, the results can be written in compact forms due to the symmetry in the combinations of the subscripts. By defining the averaging operator L as

$$L = \int_0^{2\pi} d\gamma \int_0^{\pi} d\beta \int_0^{2\pi} d\alpha \; p_n(\alpha, \beta, \gamma) \tag{C1}$$

the nonzero terms can simply be expressed as

$$L a_{uvv} a_{uvv} = 1/5 \tag{C2a}$$

$$L a_{rvv} a_{sww} = 2/15 \tag{C2b}$$

$$L a_{uvv} a_{uww} = L a_{uvw} a_{uvw} = L a_{uvw} a_{uwv}$$

$$= L a_{uww} a_{vww} = 1/15 \tag{C2c}$$

$$L a_{rvw} a_{svw} = L a_{rvw} a_{swv} = -1/30 \tag{C2d}$$

where subscripts r, s, u, v, or w can be x, y, or z. Following are some examples:

$$\int_0^{2\pi} d\gamma \int_0^{\pi} d\beta \int_0^{2\pi} d\alpha \; p(\alpha, \beta, \gamma) a_{xxx} a_{xxx} = 1/5 \tag{C3a}$$

$$\int_0^{2\pi} d\gamma \int_0^{\pi} d\beta \int_0^{2\pi} d\alpha \; p(\alpha, \beta, \gamma) a_{xxx} a_{yyy} = 2/15 \tag{C3b}$$

$$\int_0^{2\pi} d\gamma \int_0^{\pi} d\beta \int_0^{2\pi} d\alpha \; p(\alpha, \beta, \gamma) a_{xxx} a_{zxx} = 1/15 \tag{C3c}$$

$$\int_0^{2\pi} d\gamma \int_0^{\pi} d\beta \int_0^{2\pi} d\alpha \; p(\alpha, \beta, \gamma) a_{yxy} a_{xxy} = -1/30 \tag{C3d}$$

Acknowledgments. The research described in this paper was carried out by the Jet Propulsion Laboratory, California Institute of Technology, and was sponsored by the Office of Naval Research and the National Aeronautics and Space Administration and by the Massachusetts

Institute of Technology, under contracts N00014-89-J-1107 and N00014-92-J-4098 with the Office of Naval Research.

References

Arcone, S. A., A. J. Gow, and S. G. McGrew, Structure and dielectric properties at 4.8 and 9.5 GHz of saline ice, *J. Geophys. Res.*, *91*(C12), 14,281–14,303, 1986.

Colbeck, S. C., Statistics of coarsening in water-saturated snow, *Acta Metall.*, *34*(3), 347–352, 1986.

Colbeck, S. C., Snow metamorphism and classification, in *Seasonal Snowcovers: Physics, Chemistry, Hydrology*, edited by H. G. Jones and W. J. Orville-Thomas, pp. 1–35, D. Reidel Publ. Co., Norwell, Mass., 1987.

Davis, R. E., and J. Dozier, Stereological characterization of dry alpine snow for microwave remote sensing, *Adv. Space Res.*, *9*(1), 245–251, 1989.

Ding, K. H., and L. Tsang, Effective propagation constants in media with densely distributed dielectric particles of multiples sizes and permittivities, in *Progress in Electromagnetics Research, vol. 1*, chap. 3, edited by J. A. Kong, pp. 241–295, Elsevier, New York, 1989.

Lang, R. H., R. Landry, Ö. Kiliç, N. Chauhan, N. Khadr, and D. Leckie, Effect of species structure and dielectric constant on C-band forest backscatter, paper presented at International Geoscience and Remote Sensing Symposium, Tokyo, Japan, Aug. 18–21, 1993.

Maykut, G. A., Large-scale heat exchange and ice production in the central Arctic, *J. Geophys. Res.*, *87*(C10), 7971–7984, 1982.

Nghiem, S. V., M. Borgeaud, J. A. Kong, and R. T. Shin, Polarimetric remote sensing of geophysical media with layer random medium model, in *Progress in Electromagnetics Research, vol. 3: Polarimetric Remote Sensing*, chap. 1, ed. by J. A. Kong, pp. 1–73, Elsevier, New York, 1990.

Nghiem, S. V., T. Le Toan, J. A. Kong, H. C. Han, and M. Borgeaud, Layer model with random spheroidal scatterers for remote sensing of vegetation canopy, *J. Electromagn. Waves Appl.*, *7*(1), 49–76, 1993a.

Nghiem, S. V., R. Kwok, J. A. Kong, and R. T. Shin, A model with ellipsoidal scatterers for polarimetric remote sensing of anisotropic layered media, *Radio Sci.*, *28*(5), 687–703, 1993b.

Nghiem, S. V., R. Kwok, S. H. Yueh, J. A. Kong, M. A. Tassoudji, C. C. Hsu, A. J. Gow, and D. K. Perovich, Polarimetric backscattering signatures from thin saline ice under controlled laboratory conditions, paper presented at International Geoscience and Remote Sensing Symposium, Pasadena, Calif., Aug. 8–12, 1994.

Perovich, D. K., and J. A. Richter-Menge, Surface characteristics of lead ice, *J. Geophys. Res.*, *99*(C8), 16,341–16,350, 1994.

Sihvola, A. H., and J. A. Kong, Effective permittivity of dielectric mixtures, *IEEE Trans. Geosci. Remote Sens.*, *26*(4), 420–429, 1988.

Stiles, W. H., and F. T. Ulaby, The active and passive microwave response to snow parameters, 1, Wetness, *J. Geophys. Res.*, *85*(C2), 1037–1044, 1980.

Stogryn, A., An analysis of the tensor dielectric constant of sea ice at microwave frequencies, *IEEE Trans. Geosci. Remote Sens.*, *25*(2), 147–158, 1987.

Thomas, R. H., R. A. Bindschadler, R. L. Cameron, F. D. Carsey, B. Holt, T. J. Hughes, C. M. W. Swithinbank, I. M. Willans, and H. J. Zwally, Satellite remote sensing for ice sheet research, *NASA Tech. Memo. 86233*, 1985.

Tinga, W. R., W. A. G. Voss, and D. F. Blossey, Generalized approach to multiphase dielectric mixture theory, *J. Appl. Phys.*, *44*(9), 3897–3902, 1973.

Tjuatja, S., A. K. Fung, and J. Bredow, A scattering model for snow-covered sea ice, *IEEE Trans. Geosci. Remote Sens.*, *30*(4), 804–810, 1992.

Tsang, L., and J. A. Kong, Scattering of electromagnetic waves from random media with strong permittivity fluctuations, *Radio Sci.*, *16*(3), 303–320, 1981a.

Tsang, L., and J. A. Kong, Application of strong fluctuation random medium theory to scattering from vegetation-like half space, *IEEE Trans. Geosci. Remote Sens.*, *19*(1), 62–69, 1981b.

Tsang, L., J. A. Kong, and R. W. Newton, Application of strong fluctuation random medium theory to scattering of electromagnetic waves from a half-space of dielectric mixture, *IEEE Trans. Antennas Propag.*, *30*(2), 292–302, 1982.

Tsang, L., K. H. Ding, and B. Wen, Polarimetric signatures of random discrete scatterers based on radiative transfer theory, in *Progress in Electromagnetics Research, vol. 3: Polarimetric Remote Sensing*, chap. 2, edited by J. A. Kong, pp. 75–142, Elsevier, New York, 1990.

Wait, J. R., Effective electrical properties of heterogeneous earth models, *Radio Sci.*, *18*(1), 19–24, 1983.

Wait, J. R., Complex resistivity of the earth, in *Progress in Electromagnetics Research, vol. 1*, chap. 1, edited by J. A. Kong, pp. 1–173, Elsevier, New York, 1989.

Weeks, W. F., and S. F. Ackley, *The Growth, Structure, and Properties of Sea Ice, Monogr. Ser.*, vol. 82-1, U.S. Army Corps of Eng., Cold Regions Res. and Eng. Lab., Hanover, N. H., 1982.

Yueh, H. A., R. T. Shin, and J. A. Kong, Scattering from randomly oriented scatterers with strong permittivity fluctuations, *J. Electromagn. Waves Appl.*, *4*(10), 983–1004, 1990.

C. C. Hsu, J. A. Kong, R. T. Shin, and M. A. Tassoudji, Department of Electrical Engineering and Computer Science and Research Laboratory of Electronics, Massachusetts Institute of Technology, Cambridge, MA 02139.

R. Kwok, S. V. Nghiem, and S. H. Yueh, Jet Propulsion Laboratory, MS 300-235, California Institute of Technology, 4800 Oak Grove Drive, Pasadena, CA 91109. (e-mail: nghiem@malibu.jpl.nasa.gov)

(Received November 29, 1994; revised April 13, 1995; accepted April 18, 1995.)